PHYSICAL REVIEW B **82**, 104113 (2010)

Spherical solid He nanometer bubbles in an anisotropic complex oxide

Avishai Ofan,[1,*] Lihua Zhang,[2] Ophir Gaathon,[1] Sasha Bakhru,[3] Hssaram Bakhru,[3] Yimei Zhu,[2] David Welch,[2] and Richard M. Osgood, Jr.[1]
[1]*Center for Integrated Science and Engineering, Columbia University, New York, New York 10027, USA*
[2]*Brookhaven National Laboratory, Upton, New York 11973, USA*
[3]*College of Nanoscale Science and Engineering, State University of New York at Albany, Albany, New York 12222, USA*

(Received 7 March 2010; revised manuscript received 16 August 2010; published 20 September 2010; corrected 28 September 2010)

We show, using room temperature, high-resolution electron microscopy studies, that implanted He in $LiNbO_3$ nucleates and accumulates as bubbles. These He inclusions are at ~20 GPa pressure and most probably in the solid phase. In addition, the energetically favored shape of the inclusions in their as-implanted form is spherical and not oblate; this spherical shape is due to the fact that their diameter is below a critical radius for balancing the surface and elastic energies as predicted by elastic theory. When annealed, the characteristic length scale of the He inclusions increases, forming faceted bubbles. Annealing also causes the He inclusions to migrate and accumulate into strings due to the preferred $\{10\bar{1}4\}$-pyramidal-twinning planes.

DOI: 10.1103/PhysRevB.82.104113 PACS number(s): 61.82.Ms, 61.72.Qq, 68.55.Ln, 77.84.Ek

I. INTRODUCTION

Because of their extremely low solubility, impurity helium (He) atoms are known to nucleate as interstitial defects in metal crystals.[1–5] In fact, at temperatures, for which helium interstitial atoms are mobile within the lattice of the fixed host, a condition valid at 300 K,[1] the accumulation of He interstitial atoms into bubbles leads to extremely high He pressures within these bubbles, which are close to the crystal's theoretical shear strength. Thus a major goal in the study of He-implantation-induced crystal lattice changes has been to determine the atomic-level material physics of the formation of these buried defects and bubbles. This physical understanding has had important implications for a variety of technological applications involving irradiated metals. Further, the balancing of surface and volumetric energies may influence not only the size but also the shape of these nanoscale inclusions. More recently this phenomenon has been the subject of new experimental and theoretical studies, which show that He-bubble physics is also important in semiconductors. Thus extensive recent work has been reported on the detailed enabling physics of the shape, gas density, and size of He (or H) implantation-induced bubble formation in Si and SiC.[6–12] Given this background, it would be of fundamental interest to extend the understanding of the atomic-scale He inclusions to complex oxides, since these crystals offer a wide variation in mechanical, ionic, and dielectric properties. From a practical viewpoint, He inclusions in complex oxides are also important because of the importance of He implantation in a variety of fabrication strategies for microelectronic and optical devices.[13–18]

Lithium niobate ($LiNbO_3$) is a particular case in point of the importance of He implantation in ferroelectric metal oxides. This oxide has attractive optical properties and hence is widely used in a variety of active photonic devices. He implantation has been used to alter its index of refraction,[19] enhance its etch rate,[13] and enable exfoliation of single-crystal thin films from a single-crystal bulk sample.[20–22] Although many studies of He implantation in $LiNbO_3$ have been reported, to our knowledge, only two reports have shown that He implantation leads to the formation of inclusions in $LiNbO_3$.[23,24] However, no atomic-scale study and characterization of bubble-formation physics and its mechanism have been carried out. In this paper, we use high-resolution transmission electron microscopy (TEM) to probe the geometry and aspect ratio of these He-filled voids and to show how they change with post implantation annealing. Our study shows that unlike in another anisotropic crystal, SiC, implanted He in $LiNbO_3$ forms nanometer-size *spherically shaped* bubbles; then, if the ion exposure is above a critical dose or is subjected to postimplantation annealing, He aggregates into nanometer-thick strings along twinning boundaries.

II. EXPERIMENTAL DETAILS

In our experiments congruent $LiNbO_3$ *Z*-cut wafers (Crystal Technology) were diced and a dose of 5×10^{16} cm^{-2} He^+ ions at 1 MeV was then implanted along their $[000\bar{1}]$ or *Z* axis. Monte Carlo simulations [scattering and range of ions in matter (SRIM) (Ref. 25)] showed that this implantation results in a 250-nm-thick He-rich layer with an end-of-range (EOR) distance of 2.28 μm. This depth was sufficient to prevent formation of surface fissures or cracking. At its maximum, the He concentration reaches 1.76×10^{21} cm^{-3}, or 2% of the $LiNbO_3$ density, and generates a displacement of 0.45 dpa (displacement per atom); this maximum concentration occurs in the He-rich region at 2.28 μm. To prevent overheating, samples were water cooled during implantation. The temperature of the $LiNbO_3$ samples during implantation is strongly dependent on the ion-implantation current; at the conditions of our implantation ($I = 250$ nA cm^{-2}), it was measured to be ~100 °C.

The implanted crystals were prepared for cross-sectional TEM by standard slicing, polishing, and ion milling along their *X* or *Y* axis to form a wedge to give sufficient electron transparency. Since the preparation process results in residual sample heating, care was taken to limit this heating to below 130 °C to prevent spurious cracking and/or cleaving. The

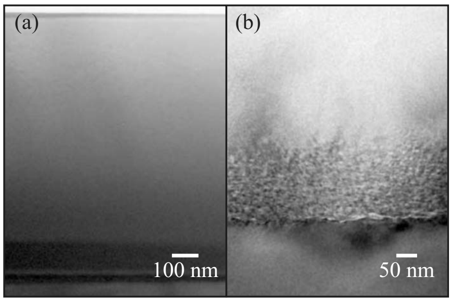

FIG. 1. TEM images at different image resolutions obtained for $LiNbO_3$ implanted with 5×10^{16} He^+/cm^2 at 1 MeV (EOR 2.28 μm), showing the implantation range (a) and the highly damaged implantation region (b).

implanted samples were analyzed using a 200 kV TEM, JEOL 2100, at the Center for Functional Nanomaterial (CFN) at Brookhaven National Laboratory (BNL).

For several of the studies below, following implantation, the crystal samples were annealed so as to examine for the effects of thermally mediated He migration or diffusion. In particular, the $LiNbO_3$ samples, which were implanted by 5×10^{16} cm^{-2} He^+ ions at 1 MeV, were annealed, after the implantation, at an ambient environment, to 350 and 400 °C. Since the annealing process caused higher brittleness of the samples, standard TEM preparation by polishing was found to result in cracking of the samples; thus following annealing, the samples were thinned down by the use of focused Ga^+ ion beam.

III. RESULTS AND DATA ANALYSIS

A. As-implanted $LiNbO_3$

Typical TEM images of He-implanted $LiNbO_3$ at low and high magnifications are shown in Figs. 1 and 2, respectively. A visual inspection of the region of maximum lattice disruption, shown in the image in Fig. 1(a), shows that the location of this plane is in excellent agreement with the stopping range calculated using the SRIM simulation discussed below. Outside of the heavily implanted region, shown in Fig. 1(b), the crystal is not perceptibly disrupted as seen in TEM images. However, in the implantation region nanometer-scale spherical voids are seen (Fig. 2); the spherical shapes of these voids were confirmed by comparing high-contrast images made along different zone axes and were seen by both optical and electron microscopy both for samples cut along their *X* and *Y* axes. No evidence of scattering of the electron flux (TEM) by the voids was seen in the images, a result that is consistent with the voids containing only low-*Z* atoms. Note that the appearance of these voids in TEM resembles the He bubbles observed in α-particle-irradiated metals.[3,26]

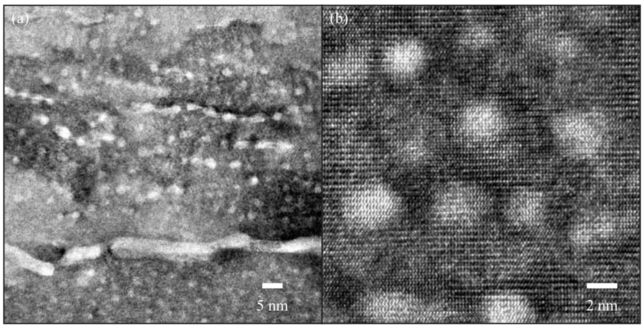

FIG. 2. High-resolution TEM images obtained for $LiNbO_3$ implanted with 5×10^{16} He^+/cm^2 at 1 MeV (EOR 2.28 μm), (a) at ×150 000 showing inclusion arrays and (b) at ×800 000 showing the spherical nature of the inclusions.

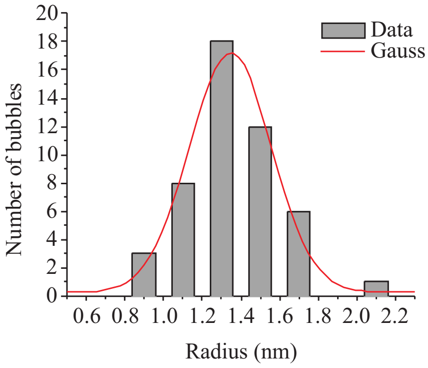

FIG. 3. (Color online) A histogram of the He inclusion's radius (histogram) and the fitted Gaussian distribution (line) of the data, giving an average radius of 1.3 ± 0.4 nm.

Our measurements using an ensemble of bubbles showed uniform He bubble shape and size distribution. In particular, the size distribution was determined by measuring the radius for bubbles in a high-contrast micrograph; a total of 48 bubbles were measured over a width (perpendicular to the surface) of 20 nm and along the entire ion trajectory. The size distribution was then fitted to a normal distribution (see histogram on Fig. 3), giving an average size of $\langle r\rangle=1.3$ nm and a variance of $\Delta r=0.4$ nm except in one narrow vertical region at the stopping range, where bubbles appeared to have coalesced into strings. Note that the detected bubble's radius has a cutoff at 0.9 nm, which is an order of magnitude bigger than the detection limit for He clusters. Thus it is clear that the entire implanted He concentration coalesced into the observed bubbles. The local average density of the He in the bubbles was determined as follows: first the thickness of the sample was measured by electron-energy-loss spectroscopy measurement to be 26 ± 3 nm. The areal number of bubbles from a region located ~0.1 μm before the stopping range was then counted in this same sample. Dividing this number of bubbles by the volume then gave a density of 10^6 bubbles/μm^3. Finally the uniformity of shape suggests that spherical shape is energetically preferred.

As predicted by our SRIM simulations, our microscopy images showed that He bubbles and implantation damage are confined to a well-defined depth. To obtain the experimental He distribution as *a function of depth*, the relative bubble concentration was counted for different depths and then compared to the distribution of implanted He concentration simulated by SRIM (Fig. 3). Both simulation and the measured distribution show a maximum concentration at a depth of 2.28 μm; note that the measured distributions show, in general, a different straggle depth between the simulated and the

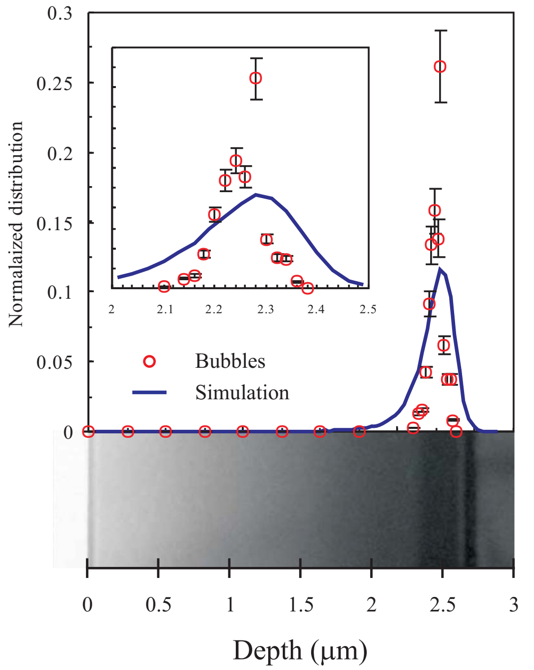

FIG. 4. (Color online) Upper panel depicts the He distribution for He^+ ions implanted in $LiNbO_3$ at 1 MeV as simulated using SRIM 2006 (blue line) and obtained from the TEM images by counting the relative bubble concentration (red circles). Inset: a zoom-in on the high He concentration region. Lower panel depicts a TEM image for comparison.

measured bubble distribution, viz., 245 and 100 nm, respectively (see inset of Fig. 3). This difference in straggling width is likely to be the result of He diffusion toward the more-vacancy-rich region, where they are trapped and then precipitate to form bubbles. The decrease in the He concentration in the vicinity of the maximum is probably a result of the coalescence of bubbles into the He "string" seen in Fig. 2(a).

Strain effects are also seen in the experiments. First, a closer examination of Fig. 2(a) indicates that the as-implanted He bubbles are arranged to form a somewhat disordered "lattice" of bubbles. In particular, visual observation of Fig. 2(a) suggests an average, mesoscopic order with bubble spacing of ~4 nm. Note that such an arrangement is not seen in lower-concentration distributions, for which the bubbles are more scattered and the average distance between bubbles is much larger than their average size. Observations also showed that once formed the spatial wavelength of bubble lattice varied inversely with the local He concentration; thus a lattice is formed with shorter wavelengths as the high local concentration increases.

B. Postimplantation annealed $LiNbO_3$

In order to further examine the behavior of the bubbles, the samples were annealed to higher temperatures. Figures 5 and 6 depict TEM images of $LiNbO_3$ samples implanted by 5×10^{16} cm^{-2} He^+ ions at 1 MeV and annealed to 350 and 400 °C, respectively, before preparation for imaging. When the sample in Fig. 5 was annealed, the He bubbles, which were already observed to exist in the implantation region after the implantation, coalesced into larger bubbles of radius ~5 nm. Our measurements of the bubble size and shape versus annealing time showed also that there was a size threshold for the formation of spherical-shaped bubbles (see discussion); thus, bubbles with a diameter >3 nm were found to be no longer spherical but rather oblate spheroids. In addition, in some cases the bubbles had straight edges or facets; these facets were oriented along the crystal basal planes. In some cases, faceting along their prismatic planes (see inset of Fig. 5) or pyramidal planes [Fig. 6(b)] was observed.

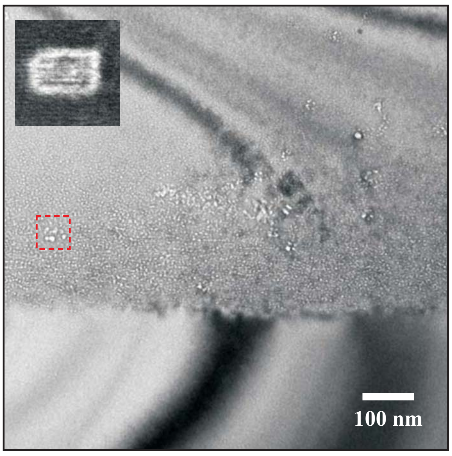

FIG. 5. (Color online) TEM image of the implantation region obtained for $LiNbO_3$ implanted with 5×10^{16} He^+/cm^2 at 1 MeV. The sample was annealed to 350 °C before imaging. At this temperature the He bubbles start to coalesce into bigger bubbles. The bright bubbles (e.g., the ones in the red box) are larger than the critical radius, r_c=2.5 nm, and are not spherical, but experience faceting along their basal and prismatic planes (inset). The size of the inset is 10×10 μm^2.

At high temperatures the He bubbles become mobile and can aggregate progressively into larger bubbles. Thus in our experiments annealing of the implanted $LiNbO_3$ samples to 400 °C resulted in aggregation of the He into bubble strings oriented along energetically preferred planes [Fig. 6(a)]. Similar aggregation was seen also for the peak He concentration in some as-implanted samples [e.g., Fig. 2(a)]. As described above, each bubble string was also found to be composed of He bubbles and was aligned along preferred orientations, namely, the basal (0001) or the pyramidal $\{10\bar{1}4\}$ planes (see below), thus forming a flat "s" shape. A detailed examination of the strings oriented along the basal plane revealed that the bubble strings were in fact composed of "steps" of bubbles also facetted along the pyramidal planes; these are readily seen in Fig. 6(b). These bubbles are ~5 nm thick (perpendicular to the twinning plane) and have a length ranging from 5 nm, in the basal-plane-faceted strings, to 20 nm, in the pyramidal-aligned strings. The bubble strings are ordered in a row parallel to the sample's surface in the region of the final ~100 nm of the implantation trajectory where the He density reaches its maximum. The spacing between adjacent He strings ranges from 100 to 200 nm.

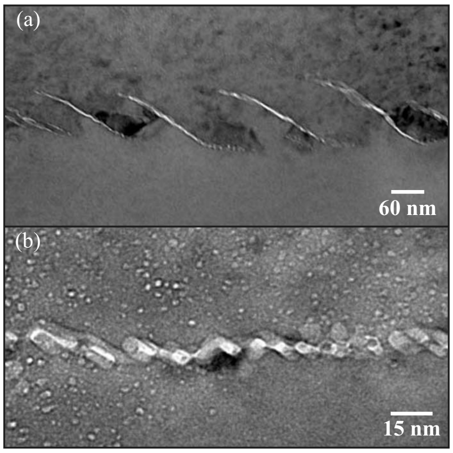

FIG. 6. TEM images of the implantation region obtained for $LiNbO_3$ implanted with 5×10^{16} He^+/cm^2 at 1 MeV. (a) The sample was annealed to 400 °C before imaging; at this temperature the He bubbles migrate and aggregate into a set of bubble strings lying on the energetically preferred basal (0001) and pyramidal $\{10\bar{1}4\}$ planes. (b) The strings oriented along the basal plane are composed of "steps" of bubbles oriented along the pyramidal planes.

It is of interest to determine the orientation of the He strings discussed above in order to understand the mechanism of the process of He coalescence. Figure 7 depicts a high-resolution TEM image of one of the He sheets seen in Fig. 6(a). The image was obtained by viewing along the $[\bar{1}\bar{1}00]$ vector and shows that the bubbles form angles of 42° with the $(\bar{1}2\bar{1}0)$ plane. This angle corresponds to the projection of the $\{10\bar{1}4\}$ twinning planes onto the imaging plane. The high stress and considerable amount of damage as a result of the high-dose implantation are known to result in defect clusters such as twinning.[27] Indeed a close examination of Fig. 7 shows that the bubble string lays on a twin boundary (marked by a dashed line) between two domains tilted at ~4°.

IV. DISCUSSION

One of the most important results of our TEM studies is that the as-implanted bubbles exhibit a clear spherical shape.

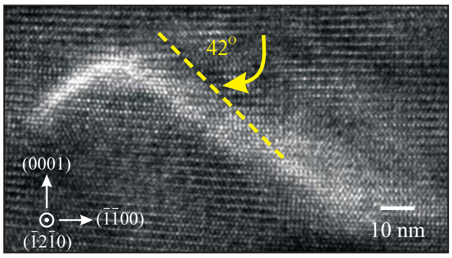

FIG. 7. (Color online) A high-resolution TEM image obtained for one of the He strings seen in Fig. 6(a). The bubbles lying on a twin boundary (marked by yellow dashed line) between two domains tilted at ~4°.

Since the shape of He bubbles is known to depend on the mechanical and the energetic properties of the solid lattice and since ionic solids such as oxides have strong crystalline anisotropy, it might be anticipated, based on the theory of elasticity,[5] that an ellipsoidal shape would occur. Indeed, it is well known that inclusions are more stable when they have oblate or needlelike shapes than spherical.[5] For example, oblate objects have been found to occur in several different crystal types, e.g., anisotropic SiC.[28] In the case of $LiNbO_3$, our measurements show that voids initially form as spheres. The shape of such inclusions is determined by consideration of their elastic and surface energies. For example, while the elastic strain energy of the inclusions can be minimized by the formation of a thin oblate or even a sheet, most likely on a cleavage plane, spherical inclusion, which has a minimum surface-to-volume ratio, lowers the surface energy of an inclusion. Since the surface energy is most important for small inclusions, there is a size threshold where an inclusion should transform from spherical to oblate or prolate shape.

A. Pressure and phase

The criterion for a spherical void as well as its physical parameters can be deduced by using elastic theory. Specifically, in the linear elastic limit, the distortion-energy density of a hollow sphere is given by

$$F = \mu(u_{rr}^2 + u_{\theta\theta}^2 + u_{\phi\phi}^2), \tag{1}$$

where u_{ii} are the strain components in spherical coordinates and the total strain is $\varepsilon = \mathbf{u}_{\mathbf{rr}} + \mathbf{u}_{\theta\theta} + \mathbf{u}_{\phi\phi}$. The strain energy is then given by

$$E_{elastic} = \int F\mathbf{dr} = \int_R^\infty F(r)4\pi r^2 dr. \tag{2}$$

Solving for deformation of a sphere with internal radius R and effective pressure P_{eff} in a matrix with a shear modulus μ yields (see Appendix)

$$E_{elastic} = \frac{\pi}{2}\frac{R^3 P_{eff}^2}{\mu}. \tag{3}$$

The effective pressure in the inclusion (P_{eff}) results from the combination of internal He pressure (P_{He}) and interfacial tension ($P_{surface}$), where P_{He} tends to expand the inclusion and $P_{surface}$ tends to constrain it,

$$P_{eff} = P_{\mathrm{He}} + P_{surface}, \tag{4}$$

Note that at equilibrium, e.g., after annealing to high temperatures, P_{eff} is zero and $|P_{\mathrm{He}}| = |P_{surface}|$, where P_{He} can be calculated from the He density inside the bubble.

The phase of implanted He has been a subject of several recent papers. As a result we discuss the possible phase for our He implants here. Specifically to obtain the He density, it is first assumed that since the samples were kept at $T < 130$ °C during the preparation for imaging such that no outdiffusion of He took place during sample preparation. The lack of He outdiffusion has also been seen earlier in our laboratory in several experiments including secondary-ionization-mass spectrometry measurements.[22] Second it is well known that the He solubility is negligible in most crystal types.[3,29] Thus it is reasonable to assume that the full implant He concentration is contained in the bubbles. Note these same assumptions have also been shown to be valid for other crystal types such as He-implanted vanadium[3] and aluminum,[29] therefore this "full-capture" assumption can be used in this calculation to obtain an upper limit calculation for the He pressure.

The He density in the bubbles can be computed from the He peak density and the bubble areal density, which was shown to be 1.76×10^{21} atoms/cm^3 and 10^6 bubbles/μm^3, respectively. The resulting He density is thus 1.6×10^{23} atoms/cm^3. At 300 K, the known He phase diagram[30] indicates that this concentration corresponds to a He pressure of ~ 20 GPa. In addition, the surface pressure can be obtained from the relation $P_{surface}=2\gamma/R$, where γ is the surface tension. If it is assumed the surface tension is that typical for metal oxides, i.e., $\gamma\sim 1\ \text{J m}^{-2}$, and a value of $P_{surface}=-1.5$ GPa is inserted in Eq. (3), it is found that $P_{eff}\sim 18.5$ GPa. At this high He density and pressure, the average distance between atoms is smaller than the van der Waals constant, i.e., He is not in gas phase. In fact, reference to the He phase diagram[31] shows that at this density He is in solid form even at room temperature. The fact that solid He is readily obtained by high-energy He implantation is surprising. A similar result had been suggested in a recent theoretical examination of high-dose He implantation in metals and SiC;[28,32] in the case of a complex oxide, it is even more striking that such high pressure exists since these crystals are comparatively brittle.

The above calculations determine the pressure of the He in the bubbles if it is assumed that the entire implanted He is formed in the bubbles. It is also interesting to determine how much He can be lost and still obtain solid-phase He. From Mao *et al.*[31] the minimum pressure needed to maintain He in the solid phase at 300 K is ~ 12 GPa; at 300 K is 12 GPa corresponds to volume of $\sim 4.2\ \text{cm}^3\ \text{mole}^{-1}$ (Ref. 30) or an atomic density of $1.4\times10^{23}\ \text{cm}^{-3}$. Hence, if one loses $<10\%$ of the implanted He, a calculation shows that the He remains in the solid phase.

B. Shape

As stated above spherical bubbles are expected only when the surface energy is comparable to the volumetric energy; this condition sets the minimum radius for spherical-bubble formation. A comparison of elastic and surface energies shows that spherical bubbles are expected only at $r_c\sim 3\gamma/\varepsilon_{elastic}$, where $\varepsilon_{elastic}=E_{elastic}/V$ is the elastic energy density and V is the bubble volume. For inclusions with $P_{eff}=18.5$ GPa and $R=1.3$ nm in a lattice with $\mu=70$ GPa, it is found that $\varepsilon_{elastic}=1.8\times10^{-9}\ \text{J m}^{-3}$ and $r_c\sim 2.5$ nm. In fact, our TEM observations showed that prior to annealing, the maximum radius for the bubbles was ~ 2 nm. Annealing resulted in coalescence of the implanted He into larger bubbles; such large-diameter bubbles are not spherical since they exceed the ~ 2.5 nm size for the balancing of surface and elastic energies. Thus $LiNbO_3$ samples annealed at $T>350$ °C formed nonspherical bubbles with radii of order 5 nm.

When annealed the equilibrium shape of the He bubbles no longer remains a sphere, as in the as-implanted case, but rather a thick He "pancake"-shaped bubble with orientation along the $\{10\bar{1}4\}$ pyramidal planes, see the image in Fig. 6. The shape of inclusions such as small solid particles in solid matrices is determined by minimization of their surface energy.[33] As a general rule, the plane of an inclusion that is normal to smaller elastic modulus will have a larger area than for the projected area in other directions. To our knowledge no detailed surface energy study has been done for $LiNbO_3$, however Wu *et al.*[34] has shown a strong correlation between the surface energy and elastic modulus, thus enabling an estimate of the surface energy ratio of the different planes using the known elastic modulus. Calculation of the surface energies for the basal, prismatic, and pyramidal planes in $LiNbO_3$ shows that the surface energy of the pyramidal facet is much higher than those of the prismatic and basal planes ($\gamma_{basal}/\gamma_{pyramid}\sim 6$ and $\gamma_{prism}/\gamma_{pyramid}\sim 3$). Thus, it is shown that the pyramidal planes are not preferred energetically as inclusion facets and another explanation should be sought. Another explanation for faceting along the pyramidal planes arises from Fig. 7, which shows that the He bubbles lay on a twin boundary. It is known that cracking and twinning in $LiNbO_3$ occurs along the $\{10\bar{1}4\}$ pyramidal planes,[35] therefore it is possible that twins form in the He-rich region as a result of the high stress in these regions. Thus, when annealed, He bubbles migrate and are trapped by the twin boundaries. In fact a careful examination of Fig. 1(c) shows that the bubbles in the He-rich region are sometimes oriented in this manner even *prior* to annealing.

The coupling of twinning and He bubbles can arise from two scenarios: local stress from defects and inclusions in the lattice are relieved via twinning, and twins, already existing in the lattice prior to the He bubbles, act as traps that catch mobile bubbles. In our case the He bubbles/twins coupling, as seen in Fig. 7, is most probably a combination of both of these scenarios. During implantation, point defects and He atoms are sufficiently mobile to freely migrate, and elastic forces between them results in clustering of defects, including the formation of He bubbles. These clusters and bubbles generate a high state of compressive stress, which is relieved primarily by mechanical twinning and to a lesser degree by dislocation nucleation and glide. The twin boundaries act as traps for secondary bubbles during implantation (see above) and for migrating bubbles during annealing.

C. Size

The uniformity of the bubble size in our sample can be explained by the strong dependency of mobility of the inclusions on their size. During the implantation process the He atoms and small bubbles are free to diffuse in the crystal matrix;[36] however their "migration velocity" is known to decrease rapidly with size ($v\sim r^{-4}$);[26] thus large bubbles are in effect stationary. Therefore at a critical radius the bubbles become immobile and are no longer small enough to freely migrate and coalesce. Consequently the bubbles have a uniform size determined by their maximum critical radius for mobility. The arrangement of the bubbles in a pseudoperiodic pattern due to strain-induced intrabubble interactions results in relatively uniform bubble spacing (see below), which at low He concentration is large, i.e., $\sim 10\ \mu\text{m}$. As a result of this large average distance between bubbles, the bubbles do not interact strongly. However at very high concentration where the average distance between bubbles is on the order of the bubble size, coalescence can form bubble strings. Such coalescence is favorable since the formation of larger inclusions leads to a reduction in interfacial energy. The uniformity of the bubble size in our samples might also be explained in light of the cascade-mixing mechanism,[36] shown to take place in metals implanted with a high dose of He ions at temperatures between $0.2T_m$ and $0.5T_m$. In this mechanism primary bubbles above a critical radius (the cascade radius) are dissolved as interstitials in the crystal by displacement cascades resulting in a higher limit to the bubble size. The dissolved He is mobile, as was stated above, and thus recoalesces into secondary bubbles smaller than the primary bubble, resulting in higher density of smaller bubbles, as was suggested by the cascade-mixing mechanism.[36]

D. Spatial distribution

As mentioned earlier, the tendency to form periodic arrangements or lattices as seen in Fig. 2(a) has been previously observed in many metal alloys (e.g., Khachaturyan and Pokrovskii[37] and Cahn[38]). In addition, in the current $LiNbO_3$ system, earlier measurements showed that He implantation leads to strain gradients.[39] Strain-induced interactions of the bubbles can be expected to arrange themselves so as to reduce total strain and thus can result in causing an overall spatial periodicity as observed here.[37,38] A second consequence of the strain distribution is also seen in the bubble coalescence described above. In particular, bubbles are found to be oriented in a plane parallel to the twinning pyramidal system $\{10\bar{1}4\}$. To summarize briefly, strain distribution can be used to arrange the bubbles in a pseudoperiodic order so as to reduce the strain field in the lattice.

V. CONCLUSIONS

In conclusion, we have shown that as-implanted He inclusions in $LiNbO_3$ contain a high-pressure He phase and show that the resulting He density is consistent with the He being in solid phase. In addition, the energetically favored shape of the as-implanted inclusions is spherical, with a radius of 1.3 nm, and not ellipsoidal as has been typically seen in other anisotropic materials. When annealed the spherical He bubbles coalesce into bubbles that are faceted along the basal, prismatic, and pyramidal planes. In addition, the bubbles migrate and accumulate into strings along a preferred pyramidal twinning-system orientation.

ACKNOWLEDGMENTS

We thank K. Kisslinger and D. Su for assistance on TEM imaging and helpful discussions. This work was supported by the NSF (Grant No. DMR-08-0668206). In addition, the research was carried out in part at the Center for Functional Nanomaterials, Brookhaven National Laboratory, which is supported by the U.S. Department of Energy, Office of Basic Energy Sciences, under Contract No. DE-AC02-98CH10886.

APPENDIX: ELASTIC THEORY OF SPHERICAL ELASTIC INCLUSIONS IN AN ISOTROPIC CONTINUUM

Voids and bubbles interact with the surrounding solid matrix according to the elastic theory. In the following appendix elastic theory is used to calculate the strain, pressure and elastic energy of spherical inclusions in the isotropic continuum.

For an elastically deformed isotropic continuum with spherically symmetric deformations the equilibrium equation for the deformations, $\mathbf{u}$, is[40]

$$\nabla(\nabla \cdot \mathbf{u}) = 0, \tag{A1}$$

giving

$$\nabla \cdot \mathbf{u} = \frac{1}{r^2}\frac{d(r^2 u)}{dr} = \text{constant} = 3a. \tag{A2}$$

The equilibrium deformations are of the form

$$u_r = ar + \frac{b}{r^2},$$

$$u_\theta = u_\phi = 0 \tag{A3}$$

and the elastic strains are

$$u_{rr} = a - \frac{2b}{r^3},$$

$$u_{\phi\phi} = u_{\theta\theta} = a + \frac{b}{r^3}, \tag{A4}$$

where a and b are constants chosen to fit the boundary conditions.

Using the boundary conditions of a hollow sphere, with external and internal radii R_1 and R_2, and pressures p_1 and p_2 inside and outside of the sphere, the constants a and b are

$$a = \frac{p_1 R_1^3 - p_2 R_2^3}{R_2^3 - R_1^3} \cdot \frac{1-2\nu}{E},$$

$$b = \frac{R_1^3 R_2^3 (p_1 - p_2)}{R_2^3 - R_1^3} \cdot \frac{1+\nu}{2E}. \tag{A5}$$

For a void with radius R containing an inner pressure p_{void} ($R_1 = R,\ R_2 = \infty,\ p_1 = 0,\ p_2 = p_{void}$), a and b become

$$a = 0, \quad b = \frac{1+\nu}{2E} R^3 p_{void} = \frac{R^3 p_{void}}{4\mu}, \tag{A6}$$

and the strains are

$$u_{rr} = -\frac{2R^3}{r^3}\frac{p_{void}}{4\mu},$$

$$u_{\theta\theta}=u_{\phi\phi}=\frac{R^3}{r^3}\frac{p_{void}}{4\mu}, \qquad \text{(A7)}$$

where $\mu=\frac{E}{2(1+\nu)}$ is the Lame's shear modulus. Note that $u_{ii}=u_{rr}+u_{\theta\theta}+u_{\phi\phi}=0$.

If the void is empty then the effective p_{void} arises from surface tension, γ. The surface energy of an empty void with radius R and deformation δ is then assumed to be

$$E_\gamma=4\pi(R+\delta)^2\gamma+\frac{d\gamma}{d\delta}\cdot\delta. \qquad \text{(A8)}$$

The term of the variation in the surface energy with strain, $\frac{d\gamma}{d\delta}\cdot\delta$, can be neglected. To the first order in $\frac{\delta}{R}$,

$$4\pi R^2 p_{void}\cdot\delta=-\frac{dE_\gamma}{d\delta}\cdot\delta \qquad \text{(A9)}$$

giving

$$p_{void}=-\frac{2\gamma}{R}. \qquad \text{(A10)}$$

If the void contains gas the gas would exert positive force on the void's surface (i.e., $p_{gas}>0$), hence the total void pressure is

$$p_{eff}=p_{gas}-\frac{2\gamma}{R}. \qquad \text{(A11)}$$

From Eqs. (A3) and (A6) we get that: $\delta=u_r=\frac{R^3 p_{void}}{R^2 4\mu}$.

Assuming the linear elasticity holds, the distortion energy density is given by[40]

$$F=\mu\left(u_{ik}-\frac{1}{3}\delta_{ik}u_{ll}\right)^2+\frac{1}{2}Ku_{ll}^2, \qquad \text{(A12)}$$

where δ_{ik} is the Kronecker delta and K is the bulk modulus. In our case, for an infinite system, $u_{ik}=0$ when $i\neq k$ and $u_{ll}=0$, therefore,

$$F=\mu(u_{ii}^2)=\mu(u_{rr}^2+u_{\theta\theta}^2+u_{\phi\phi}^2)=6\mu\frac{b^2}{r^6}. \qquad \text{(A13)}$$

The strain energy for a single bubble in an infinite matter is

$$E_{el}=\int F dV=\int_R^\infty F(r)4\pi r^2 dr=24\pi\mu b^2\int_R^\infty\frac{dr}{r^4}=8\pi\mu b^2R^{-3}$$
$$=\frac{\pi}{2}\cdot\frac{R^3p_{void}^2}{\mu}. \qquad \text{(A14)}$$

The above calculation assumes that the inclusions are spheres and the medium surrounding it is elastically isotropic. Thus, to apply these calculations to He bubbles in $LiNbO_3$ such as seen in Figs. 1 and 2, it is necessary to first ensure these assumptions are applicable. In fact as was seen in the text above, the shape of the He inclusions is uniformly spherical. In addition, due to this spherical shape one can take the elasticity to be, to first-order isotropic.

---

*ao2199@columbia.edu

[1] H. Trinkaus and B. Singh, J. Nucl. Mater. **323**, 229 (2003).
[2] K. Y. Chen and J. R. Cost, J. Nucl. Mater. **52**, 59 (1974).
[3] F. A. Smidt, Jr. and A. Pieper, J. Nucl. Mater. **51**, 361 (1974).
[4] R. S. Barnes, J. Nucl. Mater. **11**, 135 (1964).
[5] F. R. N. Nabarro, Proc. R. Soc. London, Ser. A **175**, 519 (1940).
[6] S. Leclerc, M. F. Beaufort, A. Declémy, and J. F. Barbot, Appl. Phys. Lett. **93**, 122101 (2008).
[7] X. Hebras, P. Nguyen, K. K. Bourdelle, F. Letertre, N. Cherkashin, and A. Claverie, Nucl. Instrum. Methods Phys. Res. B **262**, 24 (2007).
[8] C. H. Zhang, S. E. Donnelly, V. M. Vishnyakov, and J. H. Evans, J. Appl. Phys. **94**, 6017 (2003).
[9] B. Pivac, O. Milat, P. Dubek, S. Bernstorff, F. Corni, C. Nobili, and R. Tonini, Phys. Status Solidi A **198**, 29 (2003).
[10] M. Hartmann and H. Trinkaus, Phys. Rev. Lett. **88**, 055505 (2002).
[11] M. Luysberg, D. Kirch, H. Trinkaus, B. Holländer, S. Lenk, S. Mantl, H.-J. Herzog, T. Hackbarth, and P. F. P. Fichtner, J. Appl. Phys. **92**, 4290 (2002).
[12] J. Grisolia, G. B. Assayag, A. Claverie, B. Aspar, C. Lagahe, and L. Laanab, Appl. Phys. Lett. **76**, 852 (2000).
[13] T. Gischkat, H. Hartung, F. Schrempel, E. B. Kley, A. Tünnermann, and W. Wesch, Microelectron. Eng. **86**, 910 (2009).
[14] F. Schrempel, T. Gischkat, H. Hartung, E.-B. Kley, and W. Wesch, Nucl. Instrum. Methods Phys. Res. B **250**, 164 (2006).
[15] P. Rabiei and W. Steier, Appl. Phys. Lett. **86**, 161115 (2005).
[16] M. Levy, J. R. M. Osgood, R. Liu, L. E. Cross, I. G. S. Cargill, A. Kumar, and H. Bakhru, Appl. Phys. Lett. **73**, 2293 (1998).
[17] M. Bruel, Electron. Lett. **31**, 1201 (1995).
[18] P. J. Chandler, L. Zhang, and P. D. Townsend, Appl. Phys. Lett. **55**, 1710 (1989).
[19] P. J. Chandler, F. L. Lama, P. D. Townsend, and L. Zhang, Appl. Phys. Lett. **53**, 89 (1988).
[20] A. Guarino, G. Poberaj, D. Rezzonico, R. Degl'Innocenti, and P. Günter, Nat. Photonics **1**, 407 (2007).
[21] Y.-B. Park, B. Min, K. J. Vahala, and H. A. Atwater, Adv. Mater. **18**, 1533 (2006).
[22] A. M. Radojevic, M. Levy, R. M. Osgood, A. Kumar, H. Bakhru, C. Tian, and C. Evans, Appl. Phys. Lett. **74**, 3197 (1999).
[23] R. M. Roth, D. Djukic, Y. S. Lee, R. M. Osgood, S. Bakhru, B. Laulicht, K. Dunn, H. Bakhru, L. Wu, and M. Huang, Appl. Phys. Lett. **89**, 112906 (2006).
[24] A. Kling, M. F. da Silva, J. C. Soares, P. F. P. Fichtner, L. Amaral, and F. Zawislak, Nucl. Instrum. Methods Phys. Res. B **175**, 394 (2001).
[25] J. Ziegler, 2006, http://www.srim.org
[26] R. Barnes and D. Mazey, Proc. R. Soc. London, Ser. A **275**, 47 (1963).
[27] A. Ofan (unpublished).
[28] J. Chen, P. Jung, and H. Trinkaus, Phys. Rev. Lett. **82**, 2709 (1999).

[29] L. Koči, R. Ahuja, A. B. Belonoshko, and B. Johansson, J. Phys.: Condens. Matter **19**, 016206 (2007).

[30] P. Loubeyre, R. LeToullec, J. P. Pinceaux, H. K. Mao, J. Hu, and R. J. Hemley, Phys. Rev. Lett. **71**, 2272 (1993).

[31] H. K. Mao, R. J. Hemley, Y. Wu, A. P. Jephcoat, L. W. Finger, C. S. Zha, and W. A. Bassett, Phys. Rev. Lett. **60**, 2649 (1988).

[32] S. M. Hafez Haghighat, G. Lucas, and R. Schäublin, EPL **85**, 60008 (2009).

[33] C. Herring, Phys. Rev. **82**, 87 (1951).

[34] L. Wu, Y. Zhu, J. Tafto, D. O. Welch, and M. Suenaga, Phys. Rev. B **66**, 104517 (2002).

[35] A. M. Prokhorov and Y. S. Kuz'minov, *Physics and Chemistry of Crystalline Lithium Niobate* (Adam Hilger, Bristol, 1990), Chap. 3, p. 109.

[36] H. Trinkaus, J. Nucl. Mater. **318**, 234 (2003).

[37] A. G. Khachaturyan and B. I. Pokrovskii, Prog. Mater. Sci. **29**, 1 (1985).

[38] J. W. Cahn, Acta Metall. **10**, 179 (1962).

[39] Y. Avrahami and E. Zolotoyabko, Nucl. Instrum. Methods Phys. Res. B **120**, 84 (1996).

[40] L. D. Landau and E. M. Lifshitz, *Theory of Elasticity*, 3rd ed. (Butterworth-Heinemann, London, 1995), Chap. 1, p. 18.